Original Article

Dynamic optimisation of CO_2 electrochemical reduction processes driven by intermittent renewable energy: Hybrid deep learning approach

Xin Yee Tai [a], Lei Xing [b,*], Yue Zhang [c], Qian Fu [c], Oliver Fisher [b], Steve D.R. Christie [d], Jin Xuan [b]

[a] Department of Chemical Engineering, Loughborough University, Loughborough LE11 3TU, United Kingdom
[b] School of Chemistry and Chemical Engineering, University of Surrey, GU2 7XH, United Kingdom
[c] School of Energy and Power Engineering, Chongqing University, Chongqing 400044, China
[d] Department of Chemistry, Loughborough University, Loughborough LE11 3TU, United Kingdom

A B S T R A C T

The increasing demand for net zero solutions has prompted the exploration of electrochemical CO_2 reduction reaction (eCO_2RR) systems powered by renewable energy sources. Here, we present a comprehensive AI-enabled framework for the adaptive optimisation of the dynamic eCO_2RR processes in response to the intermittent renewable energy supply. The framework includes (1). a Bi-LSTM (bidirectional long-short-term memory) to predict the meteorological data for renewable energy input; (2). a deep learning surrogate model to predict the eCO_2RR process performance; and (3). a NSGA-II algorithm for multi-objective optimisation, targeting the trade-off of the single-pass Faraday efficiency (FE), product yield (PY) and conversion. The framework seamlessly integrates the three different AI modules, enabling adaptive optimisation of the eCO_2RR system composed of electrolyser stacks and renewable energy sources, and providing insights into system's performance and feasibility under real-world conditions.

1. Introduction

Global average atmospheric CO_2 has achieved 421 ppm in 2023, setting a new record high, which lead to global warming phenomena (N. G. M. L. US Department of Commerce, 2023). To mitigate this issue, scientists and researchers have been actively exploring carbon capture, utilisation, and storage (CCUS) technologies. One of the promising CCUS technologies is electrochemical CO_2 reduction reaction (eCO_2RR), which utilises electrical energy to convert CO_2 into single- to multi-carbon chemical and fuels and venting oxygen to the environment. Numerous techno-economy studies have indicated eCO_2RR can achieve economic feasibility for commercial use through the reduction of electrical cost and enhancements in system efficiency (Verma et al., 2019; Na et al., 2019; Rumayor et al., 2019; Verma et al., 2016; Shin et al., 2021). To enable a high eCO_2RR efficiency, many researchers focussed on the development of cost-effective and high performance electrocatalyst (Liu et al., 2020; Yang et al., 2022), optimisation of cell design and operating parameters (Gabardo et al., 2019; Tan et al., May 2020), as well as efforts to scale up eCO_2RR system (Yang et al., 2021; Endrödi et al., 2019; Siritanaratkul et al., 2022; Phillips and Dunnill, 2016). Several studies have highlighted that eCO_2RR powered by

renewable energy presents an appealing solution for reducing electricity cost (Gabardo et al., 2019, Weng et al., 2020; Weng et al., 2019), consequently enhancing the revenue generation apart from claiming subsidiary and carbon tax from government (Edwards and Celia, 2018).

To study the emerging eCO_2RR system powered by renewable energy, model-based analysis offers valuable insights into feasibility compared to experimental studies. Through the simulations, researchers can evaluate the performance and optimise various aspects of the system, including energy conversion efficiency, product selectivity, and overall system design (Yang et al., 2021; Weng et al., 2020; Weng et al., 2018). To develop a practical eCO_2RR system, the electrolyser cell is required to operate beyond a threshold current density (>100 mA cm^{-2}) to limit the electrolyser's capital cost (Shin et al., 2021). However, the competing electrochemical reactions at cathode due to suppression of eCO_2RR and promotion of hydrogen evolution reaction (HER) occurring at high current density leads to high product yield with undesirable low product selectivity. In addition, optimising stationary eCO_2RR system presents a significant challenge, but the difficulty is further amplified when optimising the system in dynamic operations with varying different power inputs due to intermittent nature of renewable energy. One approach involves combining the objectives into a unified function,

---

employing different weighting factors. However, the efficiency of weighted sum method significantly depends on the weight factors and searching for a proper weight factor can be time-consuming (Fitzpatrick et al., 2016; Krishnadasan et al., 2007; Saha et al., 2013). To overcome this issue, a robust multi-objective optimisation algorithm, namely non-dominated-sort genetic algorithm (NSGA-II), has been designed to effectively address such multiple conflicting objectives in the eCO$_2$RR systems. Sohani et al. conducted a multi-objective optimisation by using NSGA-II algorithm to optimise seven objective functions including the multi-generation system efficiency and economics viability for hydrogen generation, desalination and energy storage using solar energy (Sohani et al., 2022). The results have shown the capability of NSGA-II algorithm in resolving objectives with conflict in nature efficiently. However, the multi-objective optimisation could not be effectively performed without having a robust computation speed and high accuracy surrogate model.

With the increasing prominence of artificial intelligence (AI), machine learning (ML) has gained significant attention as a surrogate model for performance prediction which in turn facilitates in achieving effective multi-objective optimisation (Guo et al., 2021; Sun et al., 2022). Despite the recent accomplishments of data-driven ML techniques, the practical implementation for eCO$_2$RR system presents challenges. This is primarily due to scarcity of data obtained from high-throughput experiments, which is necessary to develop a reliable and comprehensive prediction model. To overcome the data limitation challenge, a promising approach is to build a hybrid model through combining the physics-based model with data-driven model. This hybrid approach leverages the strengths of both modelling techniques (Tai et al., 2022), resulting in a more comprehensive and accurate prediction framework. Many studies have reported the utilisation of physics-based model in predicting the eCO$_2$RR system performance at varying operating condition (Gabardo et al., 2019; Yang et al., 2021; Weng et al., 2020; Weng et al., 2019). Data-driven model such as ensemble model have been reported to study the impact of process parameters and catalyst type to the Faraday efficiency of eCO$_2$RR products with limited amount of experimental data (Yi et al., 2023). Nevertheless, Fan et al. demonstrated that deep neural network (DNN) outperforms ensemble model by 17% (measured in term of RMSE) when modelling complex nonlinear relationships between input and output variables (Fan et al., 2021). Additionally, hybrid models coupled with multi-objective optimisation have been discussed widely in CO$_2$ capture (Jiang et al., 2023) and storage (Pan et al., 2014). This approach has shown a promise in prediction and optimisation of improving other applications in the CCUS application, however, their application in performance optimisation in an eCO$_2$RR-based system has not been fully explored and validated yet.

Combining hybrid modelling strategy as the surrogate model with NSGA-II model creates a robust and effective AI-enabled optimisation framework, which has been widely discussed elsewhere (Tai et al., 2022; Tai et al., 2023; Xu et al., 2020). This framework potentially transforms the eCO$_2$RR system to dynamic operation via the adaptive optimisation in response to the real-time renewable energy change. However, the feasibility of eCO$_2$RR system is still hindered by the renewable energy due to its intermittent availability and make it difficult to predict. To address this challenge, a robust renewable energy prediction model is required to understand the intermittency of renewable energy by using time series model. Therefore, the predicted energy can be allocated accordingly to the electrolyser cells of the eCO$_2$RR system to avoid the waste. Recently, Bi-LSTM (bi-directional long short-term memory) which is commonly used in natural language processing (Zou et al., 2020; Ye et al., 2019; Jang et al., 2020) has gained a lot of interest in the prediction of time series data (Sun et al., 2018; Siami-Namini et al., 2019; Radhi Alharbi and Csala, 2021). Bi-LSTM is an extension of regular long short-term memory (LSTM) model. Unlike LSTM (Long short-term memory), which processes data in a single-direction, Bi-LSTM incorporate both forward and backward training data, leading to enhanced performance and improved learning. For example, Siami-Namina et al. compared the LSTM and Bi-LSTM models in

forecasting the time series data. The result shows Bi-LSTM outperforms the prediction accuracy by 37.78% compared to LSTM (Siami-Namini et al., 2019). Furthermore, Radhi Alharbi and Csala adopted Bi-LSTM to predict solar irradiation, wind speed and ambient temperature for the next 169 h with a relatively high correlation coefficient of 99, 93 and 98%, respectively (Radhi Alharbi and Csala, 2021). As demonstrated earlier, Bi-LSTM has demonstrated its capability to predict the time-series data accurately. This proficiency proves invaluable in forecasting renewable energy availability for the upcoming hour, enabling a systematic allocation of energy resources and minimising wastage.

Based on above discussion, it becomes clear that there exists a noticeable research gap when it comes to developing a comprehensive adaptive optimisation framework of eCO$_2$RR system in response to the real-time change of intermittent renewable energy. In addition, there is a lack of systematic exploration into the impact of intermittent renewable energy on the selectivity and yield of eCO$_2$RR products. Here, an AI-enabled optimisation framework is developed, employing multiphysics model to generate the database for DNN model. Subsequently, this AI model is coupled with the NSGA-II algorithm to enable multi-objective optimisation, focusing on optimising single-pass conversion, product yield and Faraday efficiency. To enable adaptive optimisation, the AI-enabled optimisation framework is employed to optimise the required number of operating electrolyser cells to offset the renewable energy input predicted by Bi-LSTM. Ultimately, it forecasts the maximum achievable total product yield. The overall framework seamlessly integrate the three different AI modules, enabling adaptive optimisation of the eCO$_2$RR system and providing insights into performance and feasibility of the eCO$_2$RR system under real-world conditions.

2. Methods

Fig. 1 demonstrates the schematic diagram of adaptive optimisation in eCO$_2$RR system, combining a renewable energy input prediction model and an AI-enabled optimisation framework. In energy input prediction architecture, Bi-LSTM is adopted to predict the time-series-wise power input based on the real time solar and wind weather conditions. The AI-enabled optimisation approach is constituted from two parts: the hybrid model and the multi-objective optimisation. In the hybrid model, a validated multiphysics model is utilised to generate the database for a deep neural network (DNN) for training and testing purposes. Then, the robust neural network is served as the surrogate model and coupled with the NSGA-II algorithm to enable the multi-objective optimisation. The single-pass Faraday efficiency (PY), product yield (PY), and conversion are chosen as the three objective functions owing to their significant influence on energy efficiency and economy viability. By integrating the real-time renewable energy prediction with AI-enabled optimisation framework, the eCO$_2$RR system enables adaptive optimisation in response to the fluctuations, effectively accommodating the intermittent and dynamic changes of renewable energy. In this section, the model development for time-series meteorological data prediction, the hybrid model for eCO$_2$RR performance prediction and the multi-objective optimisation for trade-off curve identification were discussed as follows.

2.1. System description

Our AI-based optimisation framework is demonstrated a hypothetical eCO$_2$RR system connected to both solar and wind renewable energy input. In such system, the onsite renewable energy includes a football pitch size (7140 m^2) of solar field and a wind turbine. Each solar panel and wind turbine generate a peak power of 0.41 and 3400 kW, respectively. This design gives a peak power of 4440 kW. The location of the system is assumed at Wiltshire, UK (from 1 Jan to 31 Dec 2019), where detailed meteorological data is available to build the framework (UK Met Office, 2019). The type and properties of solar panel and wind turbine are summarised in Table 1.
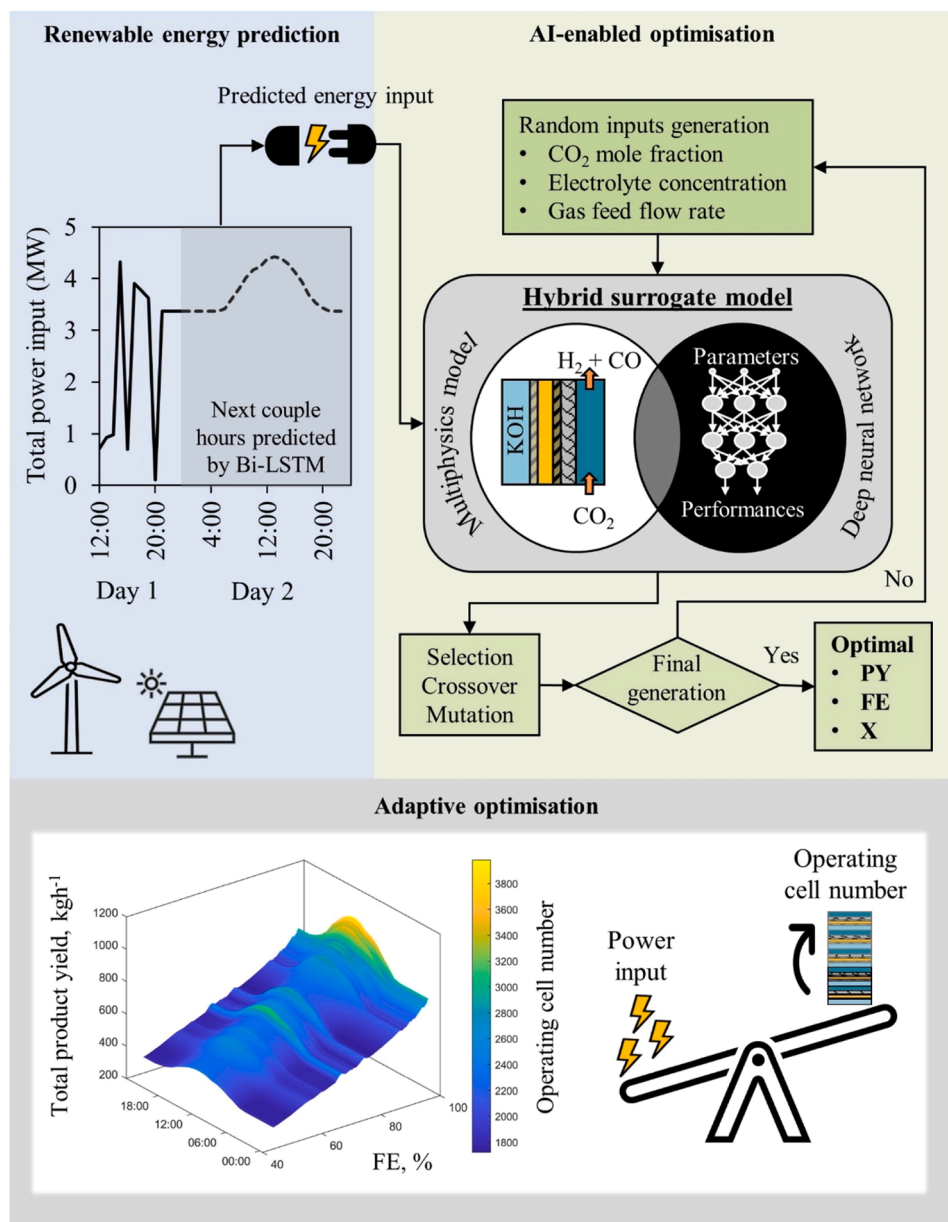
Fig. 1. Schematic diagram of adaptive optimisation of eCO$_2$RR which composed of renewable energy prediction and AI-enabled optimisation.

Table 1
Key parameters of wind turbine and solar panel.

Wind energy (Bortolotti et al., 2019)	
Wind turbine model	IEA 3.4 MW
Hub height	110 m
Rotor Diameter	130 m
Cut-in wind speed	4 m/s
Rated wind speed	9.8 m/s
Cut-out wind speed	25 m/s
Peak power	3370 kW
Ground roughness	0.03
Solar energy (JA Solar, 2023)	
Solar panel model	JA Solar JAM54S30-410/MR
Peak power	410 W
Panel length	1722 mm
Panel width	1134 mm
Solar panel yield	0.213
Performance ratio	0.75

For ease of the scale-up process, we have implemented stackable cells, instead of increasing the active area of the individual cell in the eCO$_2$RR operation. As a result, the operating cell number with the equivalent performance is dynamically optimised to efficiently utilise renewable energy input and offset its intermittent availability. According to the commercial electrolyser design, the cell able to accommodate 50 units of electrolysers with an active area of 100 cm^2 (Cawolo - Hydrogen energy, 2023). Here, the studied electrolyser is also composed of an active area of 100 cm^2. Therefore, in the following context, the term 'operating cell' refer to each cell containing 50 units of electrolyser. In certain cases, some operating cells may only be partially utilised. To simplify the analysis, we treat the partially operated cells as if they were operating at full capacity.

2.2. AI-based model for renewable energy inputs prediction

Due to the issue of intermittent availability of the wind and solar sources, a robust meteorological prediction model is required to estimate the power generation from the renewable energy sources in the

next a few hours ahead of the CO_2 electrolysers operations. A time series model, namely Bi-LSTM (bidirectional long-short-term memory) is developed to predict the wind speed and solar irradiation in the next couple of hours. The model consists of forward and backward routes and predicting the next point by evaluating the pass and future data during training process which is demonstrated in Fig. S1 in the Supplementary Information (SI). The Bi-LSTM composed two hidden layers where each hidden layer contains 100 and 75 neurons, respectively. Dropout layer with a probability of 50% is adopted to avoid overfitting. Datasets are divided into 80% and 20% for training and testing purpose. The predicted wind speed and solar irradiation are converted to wind and solar power according to power curve in Fig. S1 and Eq. (2). Given that the energy is provided in the form of current density, the power is converted to current density by dividing a constant voltage of -2.1 V applied to the electrolyser cell with the cell's cross-section area of 100 cm^2.

In the model, the measured wind speed at a height of 10 m above the ground is converted to a hub height of 110 m using the following equation.

$$v_2 = v_1 \ln \frac{h_2 - h_1}{z_0} \qquad (1)$$

where v_1 (m s^{-1}) and v_2 (m s^{-1}) are wind speeds measured from the ground height, h_1 (m) and the hub height, h_2, (m) respectively. The wind turbine is assumed to build at relative smooth surface, therefore, the ground roughness, z_0 is estimated at 0.03 (Wind Energy Concepts, 2023). The corrected wind speed is adopted to estimate the wind power (kW) from the power curve which demonstrates in Fig. S2 in the SI with the cut-in, rated and cut-out wind speeds of 4, 9.8 and 25 m s^{-1}, respectively.

Solar power (kW) is estimated by the following expression.

$$P = \frac{H \times A \times r \times PR}{t} \qquad (2)$$

where H (kJ m^{-2}), A (m^2), r, PR and t (h) represent the solar irradiation density, total area, panel yield, performance ratio and time, respectively.

2.3. AI-enabled optimisation framework for eCO$_2$RR system

Our AI-enabled optimisation framework constitutes of two parts: the hybrid model and the multi-objective optimisation loop. In the hybrid model, an experimentally validated physics-based mechanistic model is incorporated with a deep neural network (DNN) to enable better data correlation guided by a clear reflection of the process principle. The validated multiphysics model successfully generated 3067 useful data points, which were adopted as the training and testing data in the DNN. The robust hybrid model was consequently used as the surrogate model and coupled with NSGA-II algorithm to conduct multi-objective optimisation. The single-pass Faraday efficiency (FE), product yield (PY), and CO_2 conversion are optimised simultaneously, and the trade-off of the three objectives was identified from the obtained Pareto front. Pareto front is a set of solutions that are non-dominated to each other while also outperforming all other solutions within the search region.

2.3.1. Physics-based mechanistic model

Multiphysics model is developed to describe the fully coupled electrochemical reaction and transport process of mass, species, and charge in the eCO$_2$RR electrolyser cell. Fig. 2 shows the 2D computational geometry of the studied eCO$_2$RR electrolyser in the multiphysics model. The electrolyser cell consists of channels for electrolyte and gas flow, diffusion medium layer (DML) and catalyst layer (CLs) for the anode and cathode, and an anion exchange membrane (AEM) sandwiched in between. The geometrical and operating parameters of the electrolyser cell are described in Table 2.

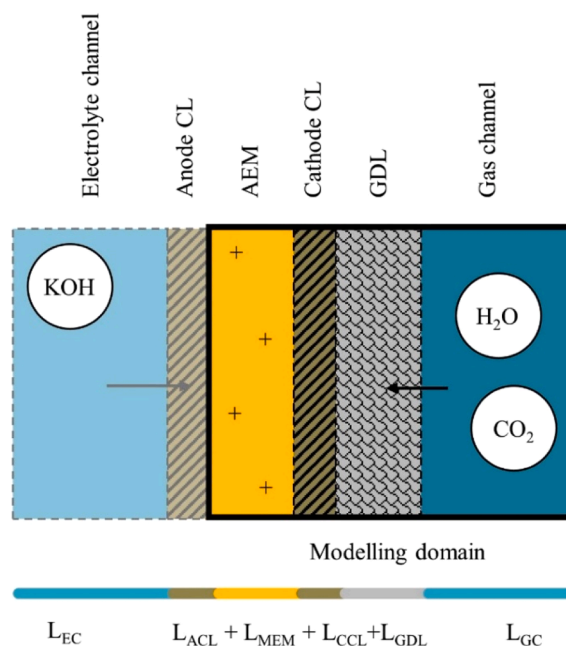At the anode, the oxygen evolution reaction (OER) is initiated by Ni

Fig. 2. Schematic diagram of CO_2 reduction electrolyser in the multiphysics interface.

Table 2
Geometrical and operating parameters of eCO$_2$RR electrolyser.

Parameters	Symbol	Unit	Value
Cell properties			
Electrode length	H_{ele}	cm	10
Electrode width	W_{ele}	cm	10
Channel thickness	L_{EC}, L_{GC}	mm	1.5
Membrane thickness	L_{MEM}	μm	50
ACL thickness	L_{ACL}	μm	100
CCL thickness	L_{CCL}	μm	20
GDL thickness	L_{DML}	μm	210
CL porosity	ε_{CL}	−	0.6
GDL porosity	ε_{GDL}	−	0.8
Standard reduction potential of H$_2$	E_{H_2}	V	−1.6
Standard reduction potential of CO	E_{CO}	V	−1.8
Charge transfer coefficient of H$_2$	α_{H_2}	−	0.15
Charge transfer coefficient of CO	α_{CO}	−	0.3
Operating condition			
Current density	i_c	mA cm^{-2}	50–200
Molar fraction of CO$_2$	y_{CO2}	−	0.1–1.0
Electrolyte concentration	M_{OH}	M	0.01–0.90
Feed gas volumetric flow rate	q_g	ml min^{-1}	20–200

catalyst, according to the following expression.

$$4OH^- \rightarrow O_2 + 2H_2O + 4e^- \qquad (3)$$

The eCO$_2$RR and hydrogen evolution reaction (HER) are catalysed by Ag cathode. Since zero-gap electrolyser with AEM membrane was used, therefore, only gas products, e.g., CO and H$_2$ are considered, owing to the very low permeation of gases through the AEM.

$$CO_2 + 2e^- + H_2O \rightarrow CO + 2OH^- \qquad (4)$$

$$2H_2O + 2e^- \rightarrow H_2 + 2OH^- \qquad (5)$$

The current density of eCO$_2$RR products, $i_{E_{co}}$ and $i_{E_{H_2}}$ are solved by using Butler–Volmer equation.

$$i_{E_{co}} = i_{0,CO} \left[\exp\left(\frac{(1 - \alpha_{CO}) F \eta_{CO}}{RT} \right) - \exp\left(\frac{-\alpha_{CO} F \eta_{CO}}{RT} \right) \right] \qquad (6)$$

$$i_{E_{H_2}} = i_{0,H_2}\left[\exp\left(\frac{(1-\alpha_{H_2})F\eta_{H_2}}{RT}\right) - \exp\left(\frac{-\alpha_{H_2}F\eta_{H_2}}{RT}\right)\right] \quad (7)$$

where F (C mol^{-1}), R (J K^{-1} mol^{-1}) and T (K) are faradic constant, gas constant and temperature. η (V) is the overpotential which defined as follow.

$$\eta_{CO} = (\phi_s - \phi_l) - E_{CO} \quad (8)$$

$$\eta_{H_2} = (\phi_s - \phi_l) - E_{H_2} \quad (9)$$

where ϕ_s (V) and ϕ_l (V) are electric potential, electrolyte potential, respectively. Standard exchange current density ($i_{0,CO}$ and i_{0,H_2}), equilibrium potential (E_{CO} and E_{H_2}) and cathodic charge transfer coefficient (α_{CO} and α_{H_2}) are summarised in Table 3.

The solid-phase electric potential, ϕ_s and liquid-phase electrolyte potential ϕ_l are solved by using charge conservation and Ohm's law.

$$Q_s = \nabla\cdot\left(-\sigma_s^{eff}\nabla\phi_s\right) \quad (10)$$

$$Q_l = \nabla\cdot\left(-\sigma_l^{eff}\nabla\phi_l\right) \quad (11)$$

where σ_s^{eff} (S m^{-1}) and σ_l^{eff} (S m^{-1}) are defined as the effective conductivities of the solid electrode and liquid electrolyte, respectively. Q_s and Q_l are the source terms, defined as follow by considering the electrochemical reactions only happen in CLs.

$$-Q_{s,CL} = Q_{l,\,CL} = a_{sl}\left(i_{E_{CO}} + i_{E_{H_2}}\right) \quad (12)$$

The electrochemical reaction rates for CO$_2$ (aq), CO and H$_2$ are expressed based on Faraday's law.

$$R_{E,CO_2(aq)} = \frac{M_{CO_2}a_{sl}(i_{CO})}{2F}; R_{E,CO} = \frac{M_{CO}a_{sl}(i_{CO})}{2F}; R_{E,H_2} = \frac{M_{H_2}a_{sl}(i_{H_2})}{2F} \quad (13)$$

where a_{sl} (m^{-1}) is the specific solid-liquid interfacial area in term of the intrinsic CL porosity, ε_{CL}^0, and the mean catalyst radius, $r_{p,CL}$ (m).

$$a_{sl} = 2\frac{\varepsilon_{CL}^0}{r_{p,CL}} \quad (14)$$

Cell voltage, product yield (PY) and Faraday efficiency (FE) were computed as the output of the physics-based mechanistic model. Product yield is an important factor to consider in the economic costs of the eCO$_2$RR system, as it measures the rates at which the desired product is produced. The desired product is specifically defined as carbon monoxide (CO), considering the impermeable AEM. CO is green feedstock for the value-added products such as methanol and gasoline. Assuming no losses of CO, the PY (kg h^{-1}) is defined as the mass of carbon monoxide per unit time for a single operating cell and is expressed as follow.

$$PY = -\frac{a_{sl}M_{CO}W_{ele}}{2F}\int_0^{H_{ele}}\int_0^{L_{CCL}} i_{E_{CO}}dx\,dy \quad (15)$$

Faraday efficiency (FE) represents the selectivity of the CO and is defined as follows.

$$FE_{CO} = \frac{a_{sl}\int_0^{H_{ele}}\int_0^{L_{CCL}} i_{E_{CO}}dx\,dy}{i_c H_{ele}} \times 100\% \quad (16)$$

where i_c (mA cm^{-2}) is the total current density which is presented as below.

$$i_c = \frac{a_{sl}\int_0^{H_{ele}}\int_0^{L_{CCL}}\left(i_{E_{CO}} + i_{E_{H_2}}\right)dx\,dy}{H_{ele}} \quad (17)$$

As one of the model outputs, the single-pass conversion is defined as PY of CO (kg h^{-1}) over the gas feed mass flow rate (kg h^{-1}), as follows.

$$X = \frac{PY}{q_g\rho_{CO_2}\times\frac{1cm^3}{1ml}\times\frac{60min}{1h}}\times 100\% \quad (18)$$

where ρ_{CO_2} (kg cm^{-3}) is the CO$_2$ density.

Multiphysics model is adopted as the database generation for training and testing in the machine learning model. The range of the studied operating condition are listed in Table 2. From the multi-physics model, a total of 3076 datasets were generated. Four design parameters, namely operating current density, molar fraction of CO$_2$, electrolyte concentration and gas feed flow rate are controlled at 50–200 mA cm^{-2}, 0.1–1.0, 0.01–0.90 M and 20–200 ml min^{-1}, respectively. Within these ranges for the design parameters, the model output give the cell voltage, PY and FE, single-pass conversion ranges at 1.895–2.797 V, 7.22–92.86%, 0.173–0.349 kg h^{-1}, 4–49% respectively.

2.3.2. Data-driven model

Data-driven models are trained and validated with the database produced by the multiphysics model. A deep neural network (DNN) with a node configuration of 10-10-10 is sandwiched in between input and output layers. The input layer is composed of four features, i.e., current density, CO$_2$ molar fraction, electrolyte concentration and gas feed flow rate while the output layer consists of cell voltage, product yield and Faraday efficiency. The output of each node is processed by rectified linear unit (ReLU) and the output layer is activated by the symmetric sigmoid transfer function in the DNN. A common machine learning cost function, namely mean square error (MSE) is adopted to calculate the average of the squared differences between the predicted and true values. Here the predicted and true values are defined as the DNN predicted results and multiphysics simulation data, respectively. To avoid overfitting, dropout technique with a probability of 50% was adopted here. The hyperparameters are tuned accordingly based on the cost function through Levenberg–Marquardt Backpropagation and then terminated when a desired error of 0.0001 is achieved. 3076 data points were divided to 70%, 15% and 15% for training, validation, and testing purposes, respectively.

2.3.3. Multi-objective optimisation

Non-dominated sorted genetic algorithm (NSGA-II) algorithm proposes a set of optimal solutions, instead of a single optimal solution through the principle of fast non-dominated sorting, sharing, elitism and crowded comparison. In the eCO$_2$RR system, the single-pass product yield is an important economic measure to assess the efficiency of CO$_2$ reduction process in the zero-gap design electrolyser. Faraday efficiency (selectivity of CO to H$_2$) and the single-pass conversion (percentage of CO$_2$ feed that is converted to products) are critical for minimising the separation requirements, and these affect both capital and operational costs. Therefore, in this multi-objective optimisation, the single-pass product yield (PY), Faraday efficiency (FE) and conversion were maximised.

The algorithm started with a random sampling of the parent population from the operating conditions, i.e., current density, CO$_2$ molar fraction, electrolyte concentration and feed flow rate of CO$_2$ with the

Table 3
Kinetic parameters for OER, HER and eCO$_2$RR to CO.

Species	Catalyst	Standard exchange current density (mA cm^{-2})	Equilibrium potential (V)	Cathodic charge transfer
O$_2$	Ni	0.9	1.1	0.4
H$_2$	Ag	1.8e−3	−0.8	0.15
CO	Ag	0.05	−0.9	0.3

range of 50–200 mA cm^{-2}, 0.1–1.0, 0.01–0.90 M and 20–200 ml min^{-1}. A crossover fraction of 0.8 is adopted here to create the offspring population and combined with the parent population to form a combined population. The corresponding model outputs, also known as objective functions, i.e., the single-pass product yield (PY), Faraday efficiency (FE) and conversion were computed based on the combined population by using the well-trained hybrid model. The objective functions were sorted and ranked based on the performance and tournament size of 2 was chosen to select the individuals from the population for reproduction. The cycle continued until the pre-defined iteration number is achieved. The maximum generation, maximum stall generation and population size are defined as 100, 100 and 500, respectively.

2.4. Adaptive optimisation of eCO$_2$RR system

To enable adaptive optimisation, renewable energy input prediction is integrated with AI-enabled optimisation framework as shown in Fig. 1. This framework provides a valuable insight into performance and feasibility of the eCO$_2$RR system under real-world conditions. In the eCO$_2$RR process, the electrolyser cells are assumed to operate at the same performance at a certain operating condition. Firstly, power consumption for a single unit of electrolyser is identified and the number of the required operating cells is computed based on the renewable power input.

To enable adaptive optimisation, optimum operating condition from the Pareto front is used to calculate the number of operating cells required to offset the renewable energy input and further identifying the total product yield. To compute the number of operating cells required, optimum power consumption is required to calculate first, as follow.

$$Power\ consumption = \phi_{s,optimum} \times i_{c,optimum} \times (H_{ele} \times W_{ele}) \times \frac{1kW}{1000W} \times \frac{1A}{1000mA}$$
$$(19)$$

$$n_{unit} = \frac{Power\ input}{Power\ consumption} \qquad (20)$$

where $i_{c,\ optimum}$ (mA cm^{-2}) is the optimum current density where it is obtained from the Pareto front, $\phi_{s,\ optimum}$ (V) is the optimum cell potential which is predicted from DNN model with the input of $i_{c,\ optimum}$, H_{ele} and W_{ele} are the dimensions of the cell, which are obtained from Table 2. The power input is defined as the solar and wind power which is predicted from Bi-LSTM algorithm. According to the commercial electrolyser design with the similar active area, one cell composed of 50 single unit of electrolyser, therefore, the operating cell number is computed as follow.

$$n_{cell} = \frac{n_{unit}}{50} \qquad (21)$$

The total product yield is the total output produced by the operating cells, which defined as follow.

$$Total\ product\ yield = n_{unit} \times PY \qquad (22)$$

where PY (kg h^{-1}) is the product yield from a single unit of electrolyser which is predicted from DNN model based optimum operating condition.

3. Result and discussion

3.1. Model validation

3.1.1. Renewable power input prediction model validation

The Bi-LSTM model was developed to predict the solar and wind energy in term of wind speed and solar irradiation, respectively, in the next couple hours, based on 24 h historic data. The wind and solar datasets from 1st to 6986th hour were used for training, while the rest of

the datasets from 6987th to 8760th were reserved for testing. For model validation, the testing datasets from 7600th to 7800th hour were chosen to compare with the predicted results from Bi-LSTM which demonstrates in Fig. 3. The solid line represents the original meteorological data, and the black dotted line is the predicted result from Bi-LSTM. Based on Fig. 3(a), the predicted result shows the great ability of the time-series model to catch the pattern of the wind speed hourly. According to Fig. 3(b), the time-series model demonstrates the capability to capture the solar irradiation density during peak periods. For example, Bi-LSTM exhibit a RMSE of 1.558 knot and 93.438 kJ m^{-2} for wind knot and solar density, respectively. However, accurately predicting periods without sunlight proves challenging for the model. This difficulty arises from the data-driven model's generalisation ability, which aims to avoid overfitting but may struggle to accurately predict periods with zero solar density. Additional work also has been done to compare the Bi-LSTM and LSTM models in predicting wind speed and solar density which demonstrates in the SI. In general, the meteorological data prediction model has demonstrated a remarkably high level of accuracy, enabling to forecast solar and wind energy output with confidence for the next few hours. Leveraging the insight, the intermittent availability of renewable energy source can be effectively managed and adapt the eCO$_2$RR system to accommodate variable power inputs.

Based on the meteorological data prediction model, the solar irradiation density and wind speed are at the range of 0–3438 kJ m^{-2} and 1–26 knot, respectively. The maximum solar irradiation density, 3438 kJ m^{-2} potentially generates 1070 kW of solar power based on the design of the football pitch solar farm. However, the maximum wind speed of 26 knot lead to 0 kW wind power due to the cut-out speed of 6 knot (equivalent to 25 m s^{-1}) at 100 m.

Fig. 4 also emphasises an important point that the integration of solar and wind energy leads to a significant reduction in the downtime when the CO$_2$ electrolysers are not supplied with energy. For example, the downtime periods would amount to 4717 and 4057 h, respectively, if wind and solar energy are adopted separately. However, by using both renewable energy sources together, the downtime is significantly
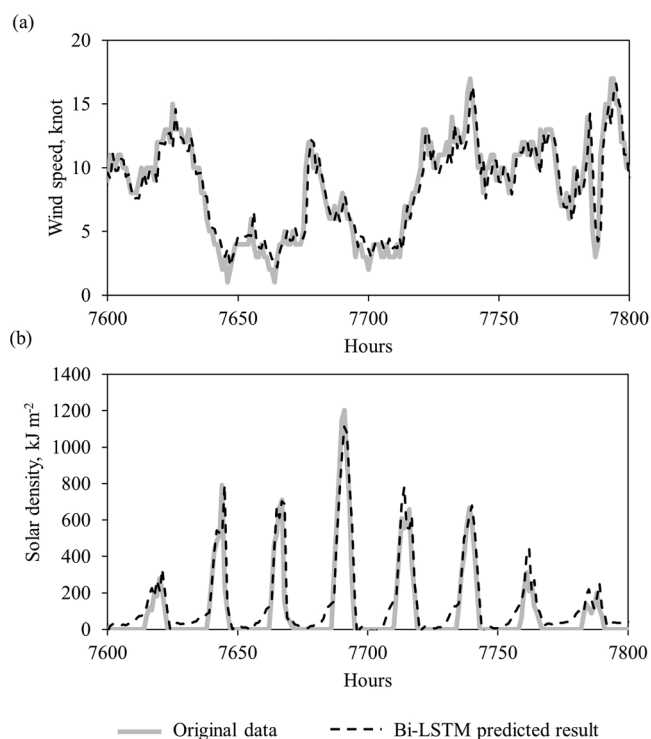

Fig. 3. Comparison of original meteorological data and prediction from Bi-LSTM time-series model for (a) wind speed and (b) solar irradiation density.
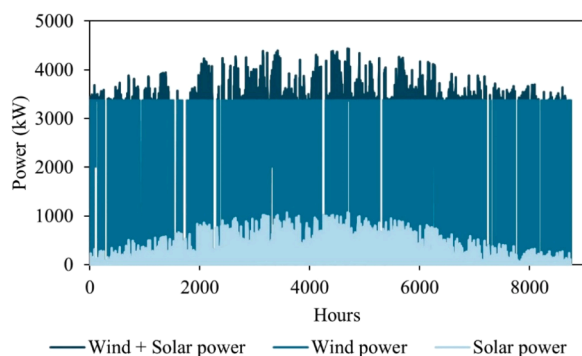
Fig. 4. Predicted power generation from wind, solar and both sources by 3600 solar panels and 1 wind turbine with peak power of 3370 kW.

reduced to 1846 h. Therefore, it is vital to consider both wind and solar energy as complementary due to the intermittent nature of renewable energy. With the installation of 3600 solar panels (equivalent to the size of 1 football pitch) and 1 wind turbine, the peak energy is raised to 4427 kW at 4718th hour according to Fig. 4, which is higher than using an individual renewable energy source (Wind and solar energy are 3370 and 1044 kW, respectively). In contrast, the integrated energy set-up gave a minimum energy of 12 kW, at 6849th hour. Therefore, the current set-up of renewable energy farm lead to a total power generation from 12 to 4427 kW.

3.1.2. Hybrid model validation—Part 1: physics-based model

The validation of the physics-based model plays a crucial role as it enables the generation of high-quality of data for the data-driven model. In accordance with experiment, the physics-based model utilised the same operating conditions, such as CO_2 molar fraction, electrolyte concentration and inlet gas flow rate at 1.0, 0.1 M and 100 ml min^{-1}, respectively, in a zero-gap electrolyser cell unit with cross-section area of 1 cm^2. The cell properties and physical parameters adopted by the physics-based model could be found in Tables 2 and 3, respectively. As shown in Fig. 5, the simulation results are in a good consistency with experimental data regarding the polarisation curve and Faraday efficiency of CO within the current density from −50 to −200 mA cm^{-2}. Good agreement is observed with RMSE of 0.076 V and 1.522% with respect to cell voltage and faraday efficiency, respectively. More details of experimental measurement are demonstrated in SI.
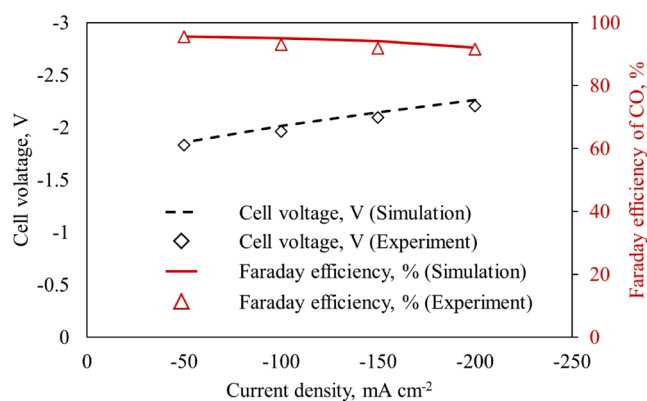
3.1.3. Hybrid model validation—Part 2: data-driven model

The prediction accuracy of the DNN model is of utmost importance as it will serve as the surrogate model in a multi-objective optimisation model. The effectiveness of the optimisation approach depends heavily on the reliability and accuracy of the surrogate model. Consequently, guaranteeing the DNN model's exceptional prediction accuracy is crucial. Therefore, a thorough validation is conducted by comparing the outcomes of the data-driven model prediction with the simulation results from the physics-based model, as shown in Fig. 6. (a) and (b) represent the comparison between DNN model and physics-based model in term of polarisation curve and Faraday efficiency and product yield and conversion, respectively, at various CO_2 mole fraction from 0.1 to 1.0 and current density from −50 to −200 mA cm^{-2}. The other operating parameters, e.g., electrolyte concentration and feed gas flow rate, are controlled at 0.1 M and 160 ml min^{-1}, respectively. Based on Fig. 6 (a) and (b), the RMSE for cell voltage, Faraday efficiency, product yield and conversion are 6.83×10^{-4} V, 0.0722%, 8.224×10^{-6} kg h^{-1}, 0.0494%, respectively. Notably, these four performance criteria exhibit an exceptionally strong correlation, with a coefficient as high as 0.9999.
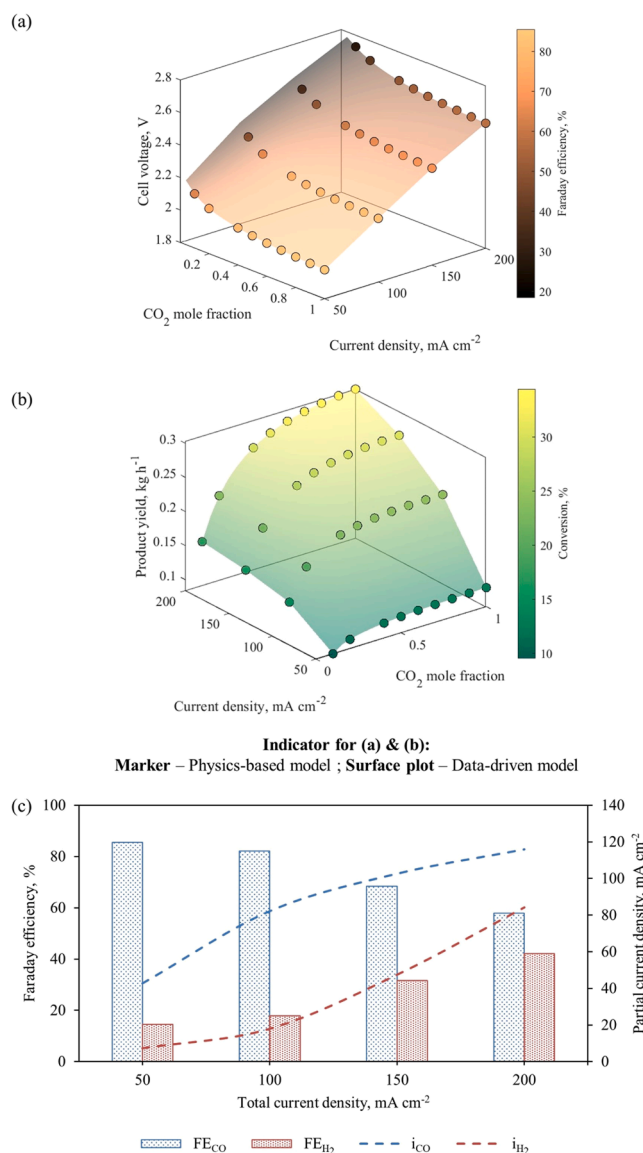

(a)

(b)

Indicator for (a) & (b):
Marker – Physics-based model ; **Surface plot** – Data-driven model

(c)

Fig. 6. Comparison of DNN with physics-based models in term of (a) polarisation curve and Faraday efficiency and (b) product yield and conversion. (c) The relationship of current density with partial current density and faraday efficiency in pure CO_2 scenario.

Fig. 5. Polarisation curve (black) and faraday efficiency (red) of physics-based model and in-house experimental data from −50 to −200 mA cm^{-2} at the CO_2 molar fraction, electrolyte concentration and inlet gas flow rate of 0.9999, 0.1 M and 100 ml min^{-1}, respectively. (For interpretation of the references to colour in this figure legend, the reader is referred to the web version of this article.)

The result reveals that, the model validation results exhibit a remarkable consistency between the DNN prediction results and the multiphysics simulation data. The DNN model demonstrates its capability capture the trade-off between the CO_2 mole fraction and the performances of the eCO_2RR system. For instant, when the current density rises, the cell voltage, PY_{CO} and single-pass conversion all exhibit an anticipated increase, while FECO experience a decrease, for all mole fraction of CO_2 in the gas inlet. This can be further explained in Fig. 6(c) that in the case of a nearly pure CO_2 inlet, the partial current density increases steeply while the partial current density of CO increases slowly after the current density reaching -100 mA cm^{-2}. This indicates that the HER dominates the eCO_2RR at high current density, leading to a low selectivity of CO and consequently, low FE_{CO}. However, with a stead increment of the partial current density of CO when the current density increases, the product yield and single-pass conversion remain increasing at the cost of low selectivity.

In addition to the current density, the validation of the model is conducted at different CO_2 mole fractions, as illustrated in the same figures. For instances, at a current density of -100 mA cm^{-2}, both models exhibit a notable enhancement in the performance of the eCO_2RR system when the CO_2 mole fraction increases, which continues to improve significantly until a CO_2 mole fraction of 0.4 is reached. Afterward, the performance improvement becomes more gradual until the maximum CO_2 mole fraction is attained. When the CO_2 mole fraction increases from 0.1 to 1.0, the performances such as FE, PY and single-pass conversion are improved by 70.246%, 70.303% and 70.246%, respectively in DNN model and by 70.231%, 70.242% and 70.231%, respectively in the physics-based model, which gives a deviation of 0.021%, 0.088% and 0.021%, respectively. The robustness of the DNN model is demonstrated by its resilience in effectively unravelling the connection between operational parameters and the performance of the eCO_2RR system, accompanied by its high precision in predicting output. Given the strong agreement observed in the model validation results, the DNN model is chosen as the surrogate model within the multi-objective optimisation framework, augmented by the NSGA-II algorithm.

3.2. System characterisations

The effect of feed gas flow rate on cell performance at various current density and a constant CO_2 mole fraction of 1.0 are shown in Fig. 7. The results in Fig. 7(a) show a significant increase in FE_{CO} higher than 35% as the feed gas flow rate increases from 50 to 200 ml min^{-1}. A higher flow rate results in a more supply of CO_2 within the flow channel, ultimately leading to a high effective CO_2 concentration in the catalyst layer and increasing the rate of reaction and FE_{CO}. However, it is important to note that when the CO_2 concentration in the catalyst layer exceed a certain limit, the electrochemical reaction begins to take precedence over mass transport in driving the overall reaction. This means that any
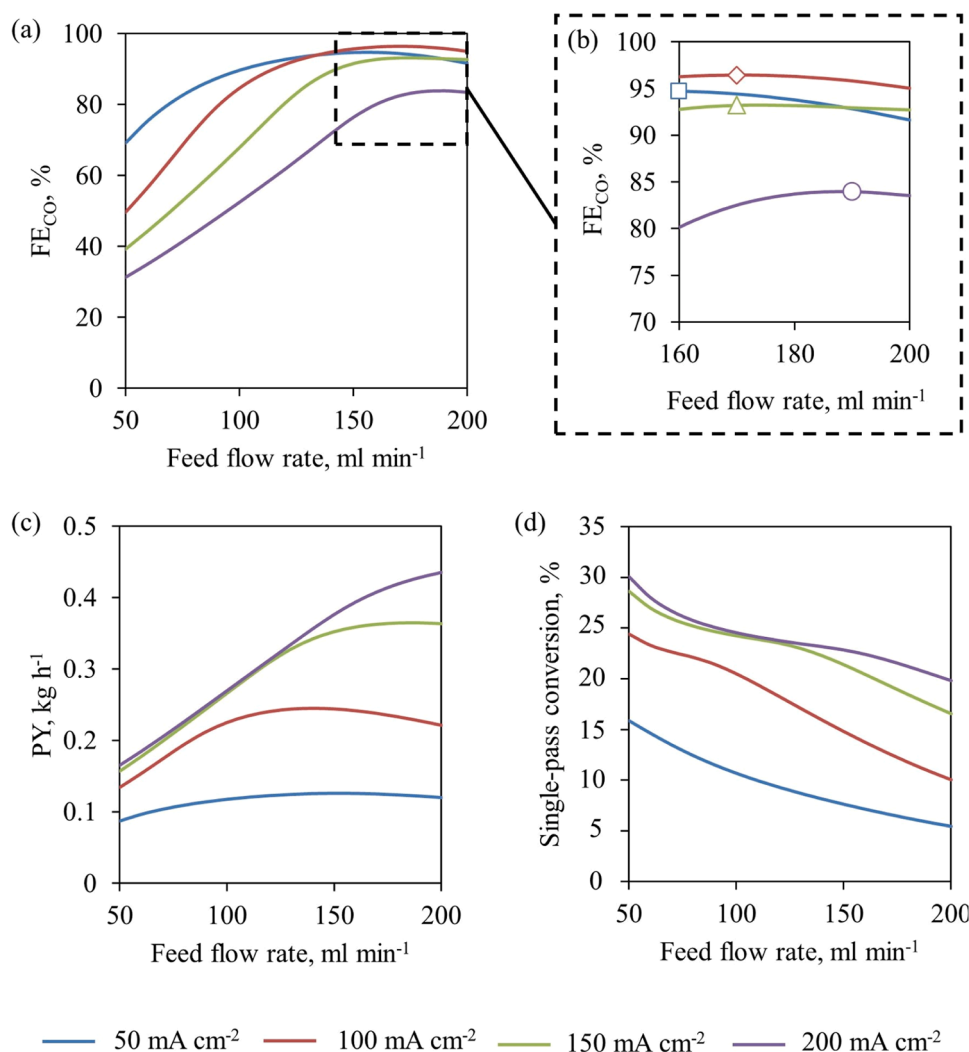

Fig. 7. Impact of feed flow rate on (a) FE$_{CO}$, (c) product yield and (d) single-pass conversion at different current density. (b) The points where FECO stop improving at the flow rate of 160, 170, 170 and 190 ml min^{-1} at the current density of 50, 100, 150 and 200 mA cm^{-2}, respectively.

subsequent increase in the CO_2 concentration have a reduced significance in dominating the reaction kinetics. For instance, at the current density of 50, 100, 150 and 200 mA cm^{-2}, the FE no longer exhibits improvement at the CO_2 flow rates of 160, 170, 170, 190 ml min^{-1}, respectively. The impact of feed flow rate on the PY is similar to that on the FE as shown in Fig. 7(c). Furthermore, a higher feed flow rate corresponds to a shorter residence time, and this decrease cannot be compensated for by the enhanced reaction kinetics, eventually resulting in a decrease in CO_2 conversion. Nevertheless, operating the electrolyser at higher feed rates, which consequently increases the throughput due to the associated advantages, e.g., reducing the operating cost by achieving a higher Faraday efficiency (FE) and lowering the capital cost by achieving a higher single-pass conversion. It is important to highlight that operating the electrolyser at different current densities but maintaining the same feed flow rate could result in similar FE_{CO}, as evident from Fig. 7(a) and (b). For example, adopting current density of 50 and 100 mA cm^{-2} with a gas feed flow rate of 130 ml min^{-1} yield the same FE_{CO} of 93%. Under the same operating conditions, the conversion and PY of CO at 100 mA cm^{-2} are higher than those at 50 mA cm^{-2}. The results in Fig. 7 indicate that under certain operating conditions, different current densities may yield the same FE of CO, but higher current density can lead to higher conversion and PY.

3.3. AI-enabled optimisation of eCO$_2$RR system

Before enabling the adaptive optimisation of the dynamic process and systems, the optimum eCO$_2$RR performance needs to be identified through AI-enabled optimisation framework. In the eCO$_2$RR system, FE, PY and conversion are the three important measures to define the energy efficiency and the economy viability. For example, high PY can lead to lesser production cost, while high FE and single-pass conversion can avoid separation requirement and thus reducing the capital and operational cost.

Fig. 8 shows the Pareto front converged by NSGA-II algorithm where each solution is improved without at the cost of the other. The trade-off curve has shown the conflicting relationship between the single-pass FE, PY and conversion. Based on Fig. 8(a), the Pareto front illustrates the optimum solutions of FE, PY and conversion at the range of 45–97%, 0.173–0.349 kg h^{-1} and 31–49%, respectively for a single cell. Notably, high FE is contributed by a low operating current density, high PY is caused by high current density and high conversion is resulted from low feed flow rate at the approximate CO_2 mole fraction and electrolyte concentration of 0.9 and 0.01 M, respectively according to Fig. 8(b). The detailed operating conditions and the corresponding maximum value of FE, PY and conversion are summarised in Table S2 in the SI. This can be explained by, when the current density increase, the PY and conversion are increased due to increase of partial current density of products. However, at higher current density, HER is dominating the eCO$_2$RR which result in more undesired products, H_2 leading to a low selectivity represented by FE.

Based on Fig. 8(a), the PY with the range of 0.173–0.349 kg h^{-1} refers to the product yield for a single operating electrolyser cell when consuming 0.02–0.04 kW of renewable power. According to the renewable energy prediction model, it is estimated to produce 12 to 4427 kW which shows in Fig. 4. Effectively accommodating this substantial amount of renewable energy necessitates the eCO$_2$RR system to operate at peak performance, as determined by the AI-enabled optimisation framework and multiply the required number of operating cells to maximise the energy consumption. This can be achieved through the adaptive optimisation where the eCO$_2$RR system is operated at its maximum performance to cope the intermittent change of renewable energy.

3.4. Adaptive optimisation of the dynamic eCO$_2$RR system

Based on the AI-enable optimisation, the Pareto front offers valuable
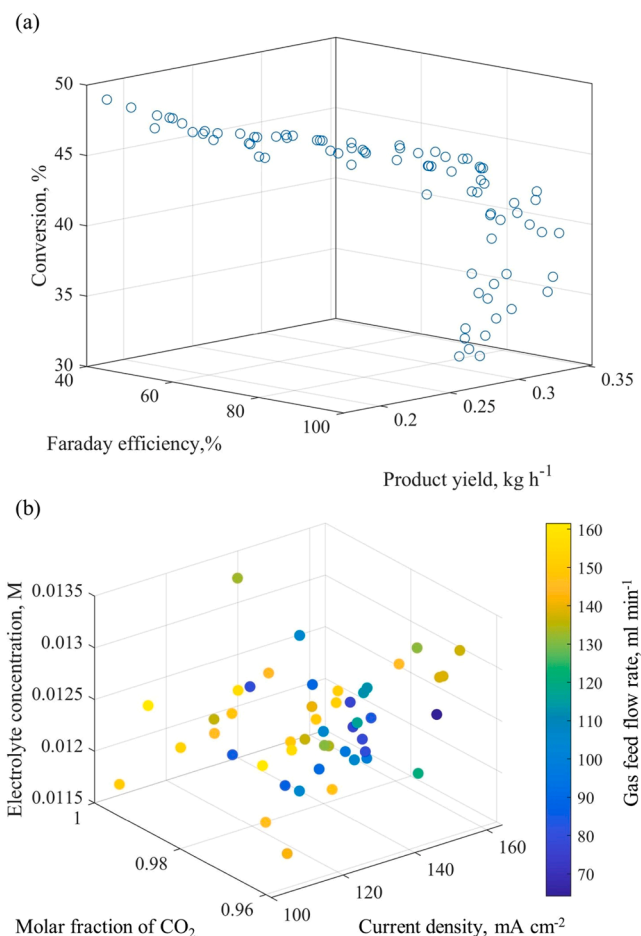

(a)

(b)

Fig. 8. (a) Pareto front converged by NSGA-II algorithm and the trade-off between FE, PY and conversion. (b) Optimum operating condition from the Pareto front.

insights into the optimal solutions for this specific type of eCO$_2$RR system, enabling the forecasting of the total product yield and dynamically adjust the operating cell number to offset the renewable power input on hourly, daily, or monthly scales. In the eCO$_2$RR, maximising FE, PY and conversion are highly desired due to energy efficiency and economy viability. In the following analysis, we have designed two scenarios to test our adaptive optimisation framework for the dynamic eCO$_2$RR system operating under different conditions, namely (1). a sunny and windy day and (2). a cloudy and still day, followed by a monthly observation and projection.

3.4.1. Scenario 1: high renewable power input days

In this scenario analysis, we choose a sunny and windy day, 16 Jul 2019. Based on the renewable energy prediction, Fig. 9(a), the eCO$_2$RR system is expected to receive a total power input of 89804 kW day^{-1}. On this particular day, the renewable power exhibits the ranges from 3370 to 4427 kW. Therefore, to leverage the predicted power input, total product yield and operating cell number are optimised to maximise the energy utilisation of the eCO$_2$RR system. Fig. 9(b)–(e) illustrate the total product yield and operating cell number distribution throughout the day based on the optimum operating condition from Fig. 8(b). In the eCO$_2$RR system, maximising FE, PY, conversion become pivotal in defining the system's energy efficiency and economy viability. Therefore, we here demonstrate three potential outcomes, representing total product yield and required number of operating cells achieved at maximum FE, PY, and conversion which illustrates in Fig. 9(d) and (e).

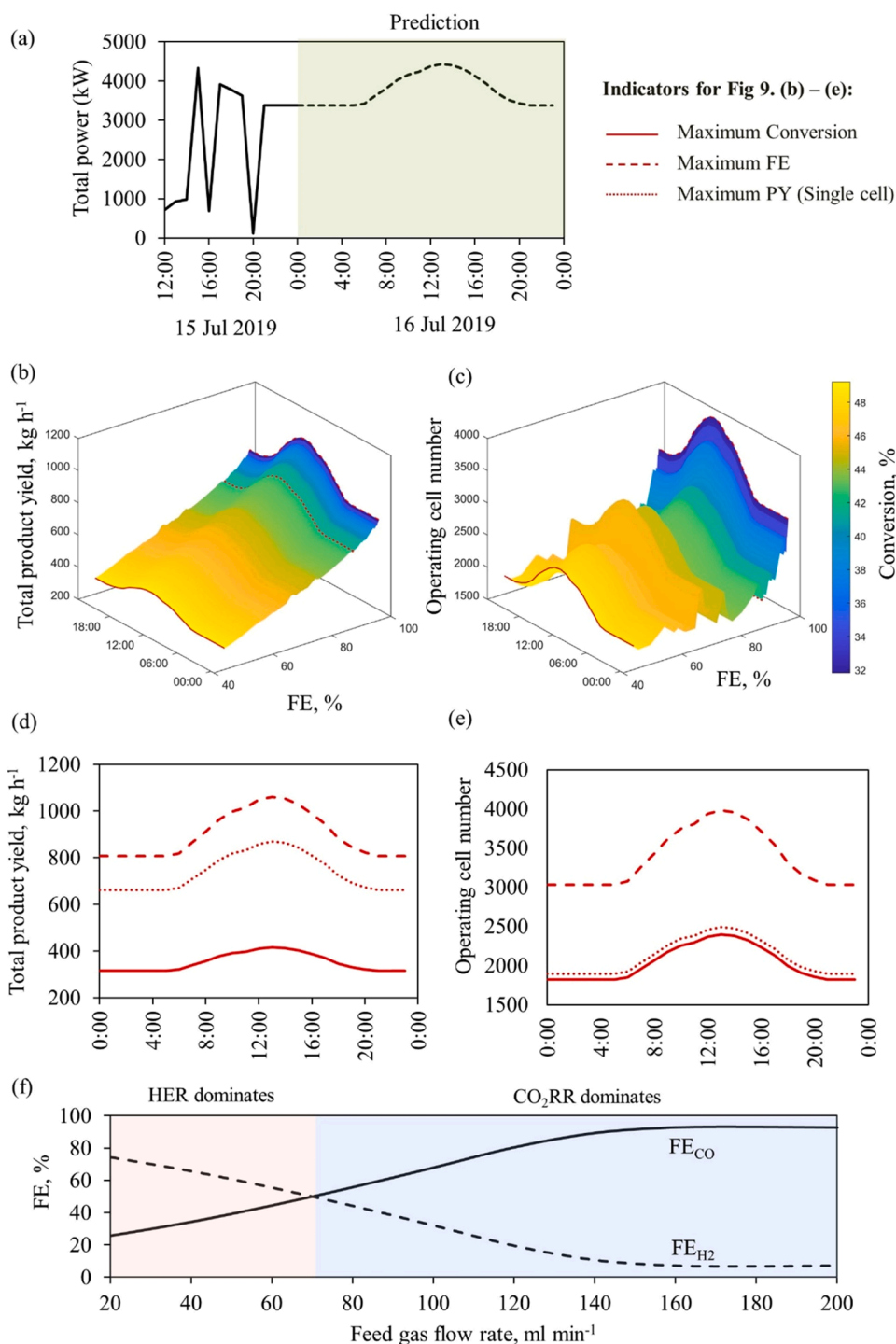Based on the results from Fig. 8(a), FE reaches a maximum value of

Fig. 9. (a) Maximum predicted renewable power input on 16 Jul 2019. The distributions of (b) total product yield and (c) operating cell number at different optimum operating conditions. (d) The total product yield and (e) operating cell number at maximum FE, PY and conversion. (f) FE for CO and H_2 impacted by the feed gas flow rate at the maximum conversion condition.

97% with a conversion of 32.1%, respectively, at the optimum operating condition of 105.6 mA cm^{-2}, 0.99, 0.01 M and 151.1 ml min^{-1}. With the power input range of 3370–4427 kW h^{-1} feeding to the eCO$_2$RR system at the optimum operating parameters, a total product yield of 807–1060 kg h^{-1} is projected to achieve with the operating cell number of 3031–3982, which illustrates as dash line in the Fig. 9(d) and (e), respectively. According to Pareto front from Fig. 8(a), maximum conversion shows 49.2% with the corresponding FE of 44.7% at the operating parameters of 148 mA cm^{-2}, 0.96, 0.01 M and 64.2 ml min^{-1}. To

achieve the maximum conversion, 1824–2396 operating cells of the CO$_2$ electrolyser is required to operate at this operating condition and estimate to produce the product at the rate of 316–416 kg h^{-1}, which demonstrates in Fig. 9(d) and (e) as the solid line. A single electrolyser cell is able to produce a maximum product yield of 0.349 kg h^{-1} at the operating condition of 154.7 mA cm^{-2}, 0.99, 0.01 M and 152.2 ml min^{-1} based on the Pareto front in Fig. 8(a). A whole-day operation of the eCO$_2$RR system at these parameters on 16 Jul 2019 leads to the production rate of 662–869 kg h^{-1} with 1845–2488 operating cells, which

show in Fig. 9(d) and (e), respectively.

It is worth to note that operating at the parameters which gave the maximum PY in a single electrolyser unit does not give the highest production rate. For example, on a windy and sunny afternoon, the product yield of highest FE and PY conditions are 1060 and 869 kg h^{-1}, respectively. When comparing two sets of operating conditions, the difference in current density become evidence. The domination of undesired HER at high current density in the maximum PY condition lead to low efficiency of conversion of CO_2 to desired product, CO. This observation indicates that current density plays a significant role in influencing the long-term total product yield. In addition, adopting

operating conditions that leads to maximum single-pass conversion exhibit the lowest product yield compared to the other two conditions. Apart from the factor of high current density, adopting low feed gas flow rate lead to low supply of CO_2 within flow channel, eventually reducing the reaction rate and FE. This can be explained by Fig. 9(f), where HER replaces the eCO_2RR and becomes the dominating process when the gas flow rate is below 70 ml min^{-1} in the highest single-pass conversion condition. To improve the FE and PY, the gas feed flow rate above 70 ml min^{-1} is desirable to suppress the HER by promoting the eCO_2RR. Compared to the highest single-pass conversion case, eCO_2RR surpasses HER at a low feed gas flow rate, e.g., 50 ml min^{-1} in the lowest single-
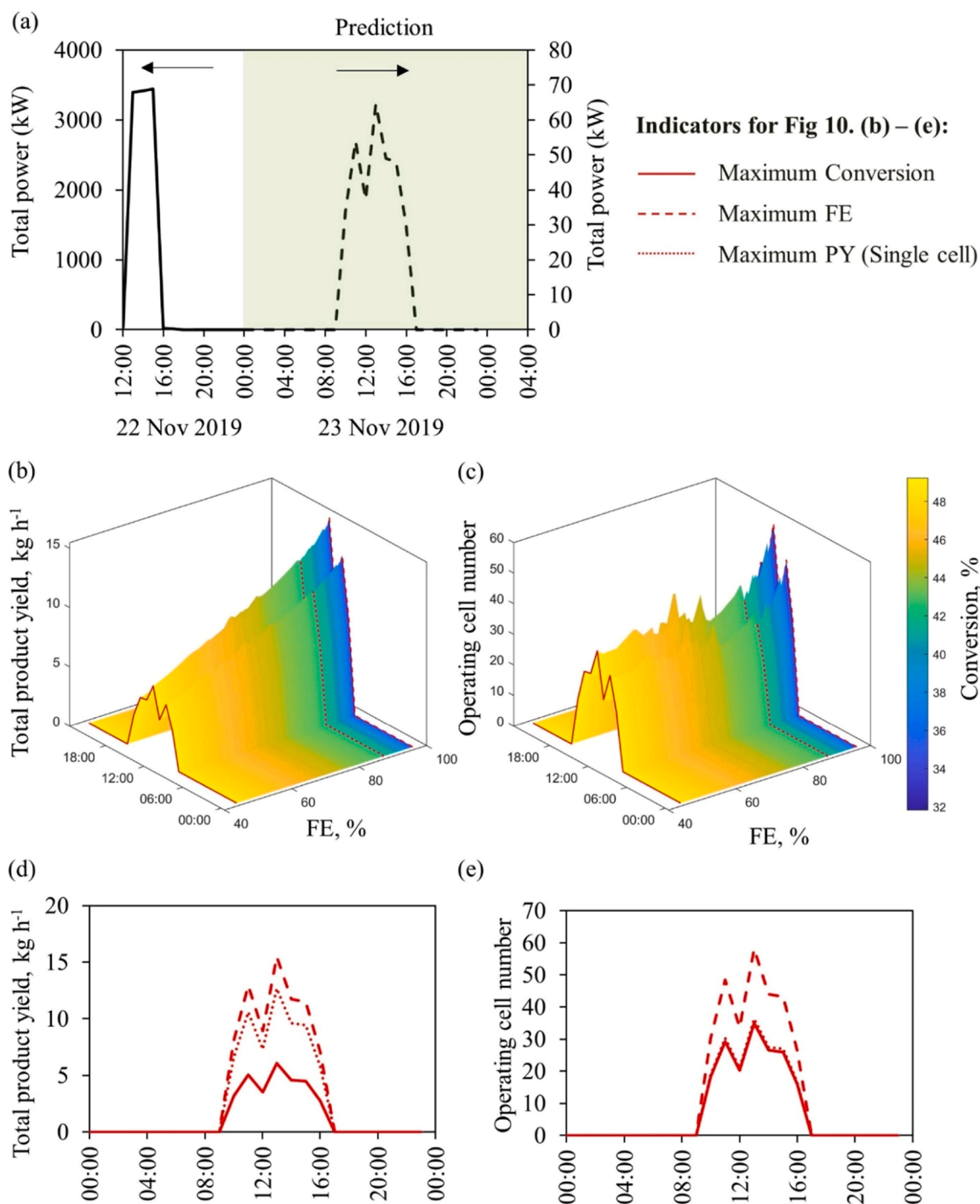

Fig. 10. (a) Distribution of the lowest power input on 23 Nov 2019. (b) Distribution of total product yield and (c) operating cell number at optimum FE and conversion. (d) Total product yield and (e) operating cell number for maximum FE, PY and conversion.

pass conversion condition. It is more beneficial to adopt low current density and high feed flow rate to achieve an acceptable range of conversion with high FE and PY. Therefore, operating consistently at the maximum FE condition on the most sunny and windy day lead to 21,515 kg of eCO$_2$RR products on the most sunny and windy day.

3.4.2. Scenario 2: low renewable input days

In this scenario, we have chosen a cloudy day on 23 Nov 2019. Based on renewable energy input prediction, it is forecasted to have the lowest total power input at 316 kW day^{-1}. On this day, the eCO$_2$RR system is estimated to receive 29.5 to 64.6 kW h^{-1} from the onsite renewable energy farm, which is demonstrated in Fig. 10(a). Therefore, low total product yield and required operating cell are expected to offset the renewable energy input on this particular day. Fig. 10(b) and (c) demonstrate the distribution of total product yield and operating cell number, respectively throughout the day. Based on the Fig. 10(b), when FE increases, the total product yield increases with a decrease of conversion. In contrast, operating cell number does not change depend on neither FE nor conversion which demonstrates in Fig. 10(c).

The distributions of total product yield and operating cell number at maximum conversion, FE and PY are illustrated in Fig. 10(d) and (e), respectively. Based on the converged Pareto front from Fig. 8(a), the maximum FE, PY and conversion for a single electrolyser are 97%, 0.349 kg h^{-1} and 49.2%, respectively. In Fig. 10(d), working on the respective operating conditions for three cases, the eCO$_2$RR product is projected to produce at the rate of 15.5, 12.7 and 6.1 kg h^{-1}, respectively, at the power input of 64.6 kW h^{-1}. With the same power input, the corresponding required operating cells are 58, 36 and 35, for maximum FE, PY and conversion, respectively, which shows in Fig. 10 (e).

The number of the required operating cells to achieve the maximum PY and conversion are very similar. However, the product yield of the maximum PY case produces 52% more CO than the maximum conversion condition. It is worth to note that the feed gas flow rate for both conditions are varying, where the maximum PY and conversion adopt 152.2 and 64.2 ml min^{-1}, respectively. Therefore, with the ignorance of current density, CO$_2$ molar fraction and electrolyte concentration, increasing feed gas flow rate enable to improve the product yield. To further improve the product yield from the maximum PY for a single electrolyser condition, adopting lower current density, which is a preferable condition for the maximum FE, leads to the increase in production yield due to the suppression of HER. Operating at moderately high current density and high feed flow rate throughout the day results in the total product yield of 76 kg on a quiet and cloudy day.

3.4.3. Adaptive modelling of intermittent renewable energy

According to the renewable energy prediction model, daily estimates range from 316 kW to 89,805 kW, translating to an hourly output of 12 kW to 4427 kW. Although the model predicts zero power input, this will be disregarded as it indicates no eCO$_2$RR operation. With the predicted power input, the AI-enabled optimisation framework is adopted to estimate the operating cell number required to leverage the power input and further project the total product yield based on the optimum conditions.

Fig. 11(a) represents the number of operating cells required to leverage the power input range from 12 to 4427 kW hourly and the corresponding total product yield at the optimum FE and conversion. The result shows that lower conversion leads to higher product yield and Faraday efficiency. In addition, more operating cells are required when the power input from renewable energy increases.

Fig. 11(b) demonstrates the predicted monthly product yield and the corresponding cumulative value for three possible conditions, e.g., the maximum conversion, PY and FE. According to previous discussion, 16 Jul 2019 is expected to be the most sunny and windy day and leads to the highest total production of the year. However, based on Fig. 11(b), the eCO$_2$RR system produces an additional 3.8, 9.8 and 8.0 MT products for
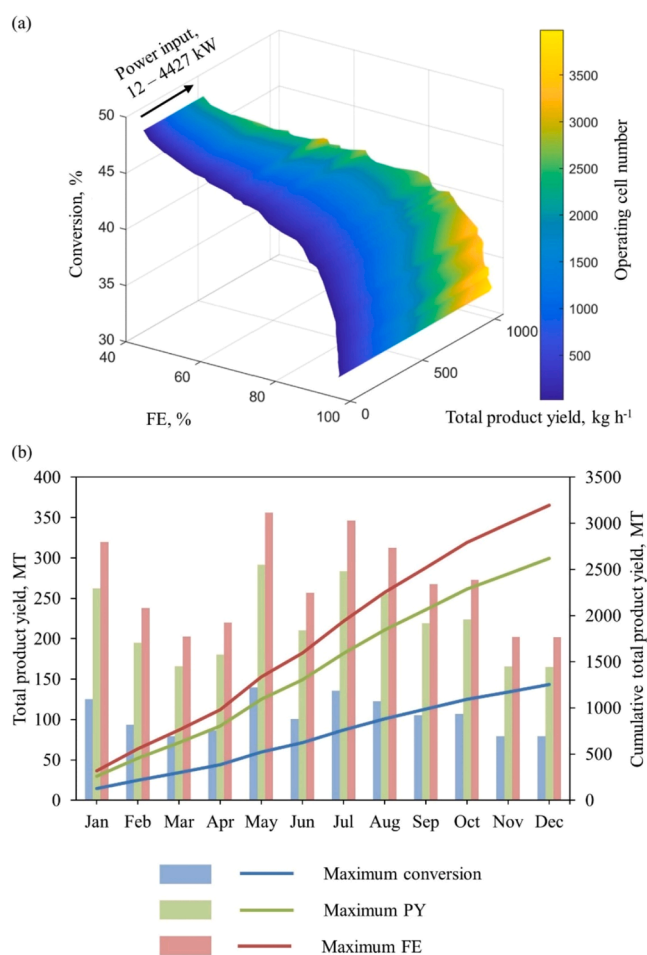

Fig. 11. (a) Total product yield and operating cell number distributions at optimum FE and conversion. (b) The monthly total product yield and cumulative total product yield from Jan to Dec 2019 at three different conditions, maximum conversion, PY and FE.

maximum conversion, FE and PY, respectively, in May compared to Jul 2019. In addition, 23 Nov 2019 is forecasted to have the lowest product yield due to lowest energy supply. According to Fig. 11(b), Dec 2019 is projected to have the lowest total product yield, demonstrating reductions of 0.2, 0.5 and 0.4 MT in highest conversion, PY and FE, respectively compared to Nov 2019.

4. Conclusion

In summary, this study presents a comprehensive framework enabling optimisation of the performance of an eCO$_2$RR system under the influence of intermittent renewable energy inputs through adaptive optimisation. The framework includes (i). a renewable energy prediction model by using Bi-LSTM and (ii). an AI-enabled optimisation model for using hybrid approach as the surrogate model in the multi-objective optimisation empowered by NSGA-II algorithm, targeting the single-pass Faraday efficiency (FE), product yield (PY) and conversion. In the renewable energy prediction model, Bi-LSTM is adopted to predict the solar and wind power in the upcoming hour based on a football pitch-size solar farm and an efficient wind turbine, enabling produced a power range from 12 to 4440 kW h^{-1} while reducing the downtime by 55–60%. To ensure the effectiveness of hybrid model in the multi-objective optimisation, the validation steps for multiphysics model and DNN models are crucial. The multiphysics model showed strong agreement with in-house experimental data (RMSE in cell voltage: 0.076V, RMSE in FE: 1.522%). While the DNN model achieved an

impressive correlation coefficient up to 99.9%, showing its remarkable consistency and ability to resolve the trade-off between operating conditions and eCO_2RR performance. Throughout the multi-objective optimisation, the resulting Pareto front reveals the relationship between improving product selectivity and compromising product yield and conversion.

To accommodate the intermittent renewable energy supply, adaptive optimisation is performed to dynamically adjust the operating cell number and identified the projected total product yield within the range of maximum and minimum FE, PY and conversion from Pareto front. Based on the renewable energy prediction, it is anticipated to have a power range of 316–89804 kW daily. By simulating the maximum FE, PY and conversion conditions on these two days, working on the operating condition (105.6 mA cm^{-2}, 0.99, 0.01 M, 151.1 ml min^{-1}) at maximum FE condition lead to the highest total product yield, 21515 kg, and 76 kg per day for peak and lowest power supply, respectively. By folding up the hourly to month energy input, it is worth to note that May exhibits the highest energy input while Dec shows the lowest power input. These two month is projected to produce the eCO_2RR product at the rate of 139.6 MT month^{-1} and 79 MT month^{-1}, respectively at the maximum FE condition. Our work provides the adaptive optimisation framework for the eCO_2RR system, accounting for intermittent influence of renewable energy and forecasting the potential outcomes based on the optimum conditions proposed by Pareto front. These findings have the potential to significantly aid the decision-making process, particularly during the start-up phase of CO_2 reduction technologies.

Declaration of Competing Interest

The authors declare that they have no known competing financial interests or personal relationships that could have appeared to influence the work reported in this paper.

Acknowledgement

Supplementary materials

Supplementary material associated with this article can be found, in the online version, at doi:10.1016/j.dche.2023.100123.

References

Bortolotti, P., et al., 2019. IEA wind TCP task 37: systems engineering in wind energy-WP2.1 reference wind turbines. Citation. https://doi.org/10.2172/1529216.

"Cawolo - Hydrogen Energy." https://albanian.gdcawolo.com/Pem-produce-hydroge n/cawolo-112kw-hydrogen-powered-electricity-generator-2-nm3h-hydrogen-pe m-electrolyzer-custom-hydrogen-electrolyzer (accessed May 11, 2023).

Edwards, R.W.J., Celia, M.A., 2018. Infrastructure to enable deployment of carbon capture, utilization, and storage in the United States. Proc. Natl. Acad. Sci. USA 115 (38), E8815–E8824. https://doi.org/10.1073/PNAS.1806504115/-/DCSUPPLEMENTAL.

Endrödi, B., et al., 2019. Multilayer electrolyzer stack converts carbon dioxide to gas products at high pressure with high efficiency. ACS Energy Lett. 4 (7), 1770–1777. https://doi.org/10.1021/ACSENERGYLETT.9B01142/ASSET/IMAGES/LARGE/NZ-2019-01142C_0007.JPEG.

Fan, J., Zheng, J., Wu, L., Zhang, F., 2021. Estimation of daily maize transpiration using support vector machines, extreme gradient boosting, artificial and deep neural networks models. Agric. Water Manag. 245, 106547 https://doi.org/10.1016/J.AGWAT.2020.106547.

Fitzpatrick, D.E., Battilocchio, C., Ley, S.V., 2016. A novel internet-based reaction monitoring, control and autonomous self-optimization platform for chemical synthesis. Org. Process Res. Dev. 20 (2), 386–394. 10.1021/ACS.OPRD.5B00313/ASSET/IMAGES/LARGE/OP-2015-003134_0016.JPEG.

Gabardo, C.M., et al., 2019. Continuous carbon dioxide electroreduction to concentrated multi-carbon products using a membrane electrode assembly. Joule 3 (11), 2777–2791. https://doi.org/10.1016/J.JOULE.2019.07.021.

Guo, Y., et al., 2021. Machine-learning-guided discovery and optimization of additives in preparing Cu catalysts for CO2 reduction. J. Am. Chem. Soc. 143 (15), 5755–5762.

https://doi.org/10.1021/JACS.1C00339/ASSET/IMAGES/MEDIUM/JA1C00339_M005.GIF.

Jang, B., Kim, M., Harerimana, G., Kang, S.U., Kim, J.W., 2020. Bi-LSTM model to increase accuracy in text classification: combining Word2vec CNN and attention mechanism. Appl. Sci. 10 (17), 5841. https://doi.org/10.3390/APP10175841.

"JA Solar JAM54S30-410/MR Solar Panel Black Frame Half Cell PV." https://www.tra desparky.com/solarsparky/solar-panels/ja-solar/mono-panels/ja-solar-jam54s30-410mr-black-frame-half-cell-solar-pv-panel (accessed Feb. 06, 2023).

Jiang, H., Wang, S., Xing, L., Pinfield, V.J., Xuan, J., 2023. Machine learning based techno-economic process optimisation for CO2 capture via enhanced weathering. Energy AI 12, 100234. https://doi.org/10.1016/J.EGYAI.2023.100234.

Krishnadasan, S., Brown, R.J.C., DeMello, A.J., DeMello, J.C., 2007. Intelligent routes to the controlled synthesis of nanoparticles. Lab Chip 7 (11), 1434–1441. https://doi.org/10.1039/B711412E.

Liu, X., Wang, Z., Tian, Y., Zhao, J., 2020. Graphdiyne-supported single iron atom: a promising electrocatalyst for carbon dioxide electroreduction into methane and ethanol. J. Phys. Chem. C 124 (6), 3722–3730. https://doi.org/10.1021/ACS.JPCC.9B11649/ASSET/IMAGES/LARGE/JP9B11649_0005.JPEG.

N. G. M. L. US Department of Commerce, Global Monitoring Laboratory - Carbon Cycle Greenhouse Gases. 2023.

Na, J., et al., 2019. General technoeconomic analysis for electrochemical coproduction coupling carbon dioxide reduction with organic oxidation. Nat. Commun. 10 (1), 1–13. https://doi.org/10.1038/s41467-019-12744-y.

Pan, I., Babaei, M., Korre, A., Durucan, S., 2014. Artificial neural network based surrogate modelling for multi- objective optimisation of geological CO2 storage operations. Energy Procedia 63, 3483–3491. https://doi.org/10.1016/J.EGYPRO.2014.11.377.

Phillips, R., Dunnill, C.W., 2016. Zero gap alkaline electrolysis cell design for renewable energy storage as hydrogen gas. RSC Adv. 6 (102), 100643–100651. https://doi.org/10.1039/C6RA22242K.

Radhi Alharbi, F., Csala, D., 2021. Wind speed and solar irradiance prediction using a bidirectional long short-term memory model based on neural networks. Energies 14, 6501. https://doi.org/10.3390/en14206501.

Rumayor, M., Dominguez-Ramos, A., Perez, P., Irabien, A., 2019. A techno-economic evaluation approach to the electrochemical reduction of CO2 for formic acid manufacture. J. CO2 Util. 34, 490–499. https://doi.org/10.1016/J.JCOU.2019.07.024.

Saha, P., Tarafdar, D., Pal, S.K., Saha, P., Srivastava, A.K., Das, K., 2013. Multi-objective optimization in wire-electro-discharge machining of TiC reinforced composite through Neuro-Genetic technique. Appl. Soft Comput. 13 (4), 2065–2074. https://doi.org/10.1016/J.ASOC.2012.11.008.

Shin, H., Hansen, K.U., Jiao, F., 2021. Techno-economic assessment of low-temperature carbon dioxide electrolysis. Nat. Sustain. 4 (10), 911–919. https://doi.org/10.1038/s41893-021-00739-x.

Siami-Namini, S., Tavakoli, N., Namin, A.S., 2019. The performance of LSTM and BiLSTM in forecasting time series. In: Proceedings - 2019 IEEE International Conference on Big Data, Big Data 2019, pp. 3285–3292. https://doi.org/10.1109/BIGDATA47090.2019.9005997.

Siritanaratkul, B., Forster, M., Greenwell, F., Sharma, P.K., Yu, E.H., Cowan, A.J., 2022. Zero-gap bipolar membrane electrolyzer for carbon dioxide reduction using acid-tolerant molecular electrocatalysts. J. Am. Chem. Soc. 144 (17), 7551–7556. https://doi.org/10.1021/JACS.1C13024/ASSET/IMAGES/LARGE/JA1C13024_0005.JPEG.

Sohani, A., et al., 2022. Dynamic multi-objective optimization applied to a solar-geothermal multi-generation system for hydrogen production, desalination, and energy storage. Int. J. Hydrogen Energy 47 (74), 31730–31741. https://doi.org/10.1016/J.IJHYDENE.2022.03.253.

Sun, Q., Jankovic, M.V., Bally, L., Mougiakakou, S.G., 2018. Predicting blood glucose with an LSTM and Bi-LSTM based deep neural network. In: 2018 14th Symposium on Neural Networks and Applications, NEUREL 2018. https://doi.org/10.1109/NEUREL.2018.8586990.

Sun, Z., et al., 2022. Machine learning accelerated calculation and design of electrocatalysts for CO2 reduction. SmartMat 3 (1), 68–83. https://doi.org/10.1002/SMM2.1107.

Tai, X.Y., Ocone, R., Christie, S.D.R., Xuan, J., 2022. Multi-objective optimisation with hybrid machine learning strategy for complex catalytic processes. Energy AI 7, 100134. https://doi.org/10.1016/J.EGYAI.2021.100134.

Tai, X.Y., Xing, L., Christie, S.D.R., Xuan, J., 2023. Deep learning design of functionally graded porous electrode of proton exchange membrane fuel cells. Energy, 128463. https://doi.org/10.1016/J.ENERGY.2023.128463.

Tan, Y.C., Lee, K.B., Song, H., Oh, J., 2020. Modulating local CO2 concentration as a general strategy for enhancing C−C coupling in CO2 electroreduction. Joule 4 (5), 1104–1120. https://doi.org/10.1016/J.JOULE.2020.03.013.

"UK Met Office," 2019. https://www.metoffice.gov.uk/ (accessed Feb. 06, 2023).

Verma, S., Kim, B., Jhong, H.R.M., Ma, S., Kenis, P.J.A., 2016. A gross-margin model for defining technoeconomic benchmarks in the electroreduction of CO2. ChemSusChem 9 (15), 1972–1979. https://doi.org/10.1002/CSSC.201600394.

Verma, S., Lu, S., Kenis, P.J.A., 2019. Co-electrolysis of CO2 and glycerol as a pathway to carbon chemicals with improved technoeconomics due to low electricity consumption. Nat. Energy 4 (6), 466–474. https://doi.org/10.1038/s41560-019-0374-6.

Weng, L.C., Bell, A.T., Weber, A.Z., 2018. Modeling gas-diffusion electrodes for CO2 reduction. Phys. Chem. Chem. Phys. 20 (25), 16973–16984. https://doi.org/10.1039/C8CP01319E.

Weng, L.C., Bell, A.T., Weber, A.Z., 2019. Towards membrane-electrode assembly systems for CO2 reduction: a modeling study. Energy Environ. Sci. 12 (6), 1950–1968. https://doi.org/10.1039/C9EE00909D.

Weng, L.C., Bell, A.T., Weber, A.Z., 2020. A systematic analysis of Cu-based membrane-electrode assemblies for CO_2 reduction through multiphysics simulation. Energy Environ. Sci. 13 (10), 3592–3606. https://doi.org/10.1039/D0EE01604G.

"Wind Energy Concepts." http://xn–drmstrre-64ad.dk/wp-content/wind/miller/windpower%20web/en/stat/unitsw.htm#roughness (accessed Feb. 06, 2023).

Xu, H., et al., 2020. Towards online optimisation of solid oxide fuel cell performance: combining deep learning with multi-physics simulation. Energy AI 1, 100003. https://doi.org/10.1016/j.egyai.2020.100003.

Yang, Y., Wang, J., Shu, Y., Ji, Y., Dong, H., Li, Y., 2022. Significance of density functional theory (DFT) calculations for electrocatalysis of N_2 and CO_2 reduction reactions. Phys. Chem. Chem. Phys. 24 (15), 8591–8603. https://doi.org/10.1039/D1CP05442B.

Yang, Z., et al., 2021. Modeling and upscaling analysis of gas diffusion electrode-based electrochemical carbon dioxide reduction systems. ACS Sustain. Chem. Eng. 9 (1), 351–361. 10.1021/ACSSUSCHEMENG.0C07387/ASSET/IMAGES/LARGE/SC0C07387_0006.JPEG.

Ye, H., Cao, B., Peng, Z., Chen, T., Wen, Y., Liu, J., 2019. Web services classification based on wide & Bi-LSTM model. IEEE Access 7, 43697–43706. https://doi.org/10.1109/ACCESS.2019.2907546.

Yi, L.J., Tsai, W.-H., Cheng, I.-C., 2023. A hybrid machine learning-genetic algorithm (ML-GA) model to predict optimal process parameters of nanoporous Cu for CO_2 reduction. Mater. Today Energy 36, 101352. https://doi.org/10.1016/J.MTENER.2023.101352.

Zou, Y., et al., 2020. A robust license plate recognition model based on Bi-LSTM. IEEE Access 8, 211630–211641. https://doi.org/10.1109/ACCESS.2020.3040238.